Monthly Notices of the ROYAL ASTRONOMICAL SOCIETY

MNRAS **517,** 4275–4290 (2022) https://doi.org/10.1093/mnras/stac2992
Advance Access publication 2022 October 20

SDSS-IV MaStar: [α/Fe] for the MaNGA Stellar Library from synthetic model spectra

Lewis Hill [1]★ Daniel Thomas [1,2] Claudia Maraston [1] Renbin Yan [3] Daniel Lazarz,[4] Yan-Ping Chen,[5] Guy S. Stringfellow [6] Michele Cappellari [7] Jon A. Holtzman,[8] Julie Imig,[8] Dmitry Bizyaev [9,10] David R. Law,[11] Keivan G. Stassun [12] and Niv Drory[13]

[1]*Institute of Cosmology and Gravitation, University of Portsmouth, Burnaby Road, Portsmouth PO1 3FX, UK*
[2]*School of Mathematics and Physics, University of Portsmouth, Lion Gate Building, Portsmouth PO1 3HF, UK*
[3]*Department of Physics, The Chinese University of Hong Kong, Shatin, N.T., Hong Kong, China*
[4]*Department of Physics and Astronomy, University of Kentucky, 505 Rose Street, Lexington, KY 40506, USA*
[5]*New York University Abu Dhabi, Abu Dhabi, PO Box 129188, United Arab Emirates*
[6]*Center for Astrophysics and Space Astronomy, University of Colorado, 389 UCB, Boulder, CO 80309, USA*
[7]*Sub-Department of Astrophysics, Department of Physics, University of Oxford, Denys Wilkinson Building, Keble Road, Oxford OX1 3RH, UK*
[8]*Department of Astronomy, New Mexico State University, Las Cruces, NM 88003, USA*
[9]*Apache Point Observatory and New Mexico State University, PO Box 59, Sunspot, NM 88349, USA*
[10]*Sternberg Astronomical Institute, Moscow State University, Universitetskij pr. 13, Moscow, 119992, Russia*
[11]*Space Telescope Science Institute, 3700 San Martin Dr., Baltimore, MD 21218, USA*
[12]*Vanderbilt University, Physics and Astronomy Department, 6301 Stevenson Center Ln., Nashville, TN 37235, USA*
[13]*McDonald Observatory, The University of Texas at Austin, 1 University Station, Austin, TX 78712, USA*

Accepted 2022 October 6. Received 2022 September 29; in original form 2022 August 3

ABSTRACT

We calculate the α-enhancement ratio [α/Fe] for the Mapping Nearby Galaxies at APO (MaNGA) Stellar Library (MaStar) while also fitting for the fundamental atmospheric parameters effective temperature, surface gravity, and metallicity – $T_{\rm eff}$, log g, [Fe/H]. This approach builds upon a previous catalogue of stellar parameters, whereby only the fundamental atmospheric parameters are fit with solar-scaled models. Here, we use the same Markov Chain Monte Carlo method with the additional free parameter [α/Fe]. Using the full spectral fitting code pPXF, we are able to fit multiple lines sensitive to [α/Fe] for a more robust measurement. Quality flags based on the convergence of the sampler, errors in [α/Fe] and a cut in the χ^2 of the model fit are used to clean the final catalogue, returning 17 214 spectra and values in the range of $-0.25 < [\alpha/{\rm Fe}] < 0.48$. Comparing our calculated [α/Fe] with literature values reveals a degeneracy in cool stars with log $g \geq \sim 4$; this comparison is then used to create an alternative and calibrated parameter set. We also plot the final catalogue in an [Fe/H] versus [α/Fe] diagram and recover the expected result of increasing [α/Fe] with decreasing [Fe/H] for Milky Way disc-halo stars. We apply our method to a subsample of spectra of uniform resolution and higher signal to noise that finds that our results are independent of this higher signal to noise. In the context of stellar population models, we are able to cover a parameter space for the creation of intermediate to old age models at solar-scaled [α/Fe], high [Fe/H] and enhanced [α/Fe], low [Fe/H].

Key words: techniques: spectroscopic – stars: abundances – stars: atmospheres – stars: evolution – stars: fundamental parameters – galaxies: stellar content.

1 INTRODUCTION

Element abundance ratios such as the enhancement of α-type elements (O, Mg, Si, Ca, and Ti) compared to Fe peak elements (V, Cr, Fe, Co) can be used to measure the chemical enrichment, star formation history, and initial mass function (IMF) of stellar populations. Aller & Greenstein (1960) and Wallerstein (1962) were the first to recognize an over overabundance of α type elements in G-type dwarfs. This was later discussed by Tinsley (1979, 1980), who suggested that α-type elements enrich the ISM from the collapse of massive stars (typically $M \gtrapprox 8\,{\rm M}_{\odot}$) as a result of Type II supernova (SNII) events occurring on short time-scales. Whereas, Fe peak elements, as well as α type, are mainly ejected from Type Ia supernova (SNIa) that occur at later times (Greggio & Renzini 1983; Nomoto, Thielemann & Yokoi 1984). This onset of SNIa is most clearly imprinted on the [Fe/H] versus [α/Fe] distribution of Milky Way (MW) stars. The [α/Fe] abundance ratio and the relative position of the 'knee' in the [Fe/H] versus [α/Fe] diagram can be used to infer star formation history and to probe the IMF as more massive stars will lead to elevated levels of α-type elements, leading to a higher plateau at low metal enrichment before the onset of SN1a (Matteucci

★ E-mail: lewis.hill@port.ac.uk

1994; Thomas, Greggio & Bender 1999; Thomas et al. 2005). When considering the different stellar populations of the bulge, thin/thick disc or halo of the MW, the α enhancement has been shown to vary due to the different formation time-scales and can shed light on how these components have formed (Gonzalez et al. 2011; Navarro et al. 2011; Hayden et al. 2015; Ness & Freeman 2016; Duong et al. 2019; Nissen et al. 2020).

When developing stellar population models for the purpose of studying the properties of stellar systems, in particular those with subsolar metallicities, it is imperative to consider the [α/Fe] of the input stellar spectra and the stellar evolutionary tracks. The stellar evolutionary tracks are used in evolutionary population synthesis to describe the energetics of main-sequence stars and link the parameters of observed spectra to the theoretical parameters expected for different stellar evolutionary phases (Maraston 1998, 2005). It has been shown that [α/Fe] enhancement directly affects the stellar tracks by making them hotter at a given luminosity, with the difference increasing with metallicity (Salasnich et al. 2000; VandenBerg et al. 2000; Pietrinferni et al. 2006; Fu et al. 2018). This is a result of higher mean opacities in the solar-scaled stars causing steeper radiative temperature gradients and a lower $T_{\rm eff}$. Furthermore, Gustafsson et al. (2008) show that an α enhancement can significantly affect the temperature-pressure structures for cool giants and dwarfs at $T_{\rm eff} < 4500$ K. Due to surface heating from the increased Ti abundance and back warming effects from TiO absorption, $T_{\rm eff}$ can be increased by as much as $\sim$10 per cent in dwarfs and by $\sim$5 per cent in giants, compared to the solar-scaled equivalent model atmosphere. Therefore, by only using solar-scaled models, one is biased to older ages when analysing stellar systems of sub-solar metallicity.

In fig. 6 of Maraston et al. (2003), the effect of using [α/Fe] enhanced stellar tracks at a fixed metallicity in simple stellar population (SSP) models is explored. They show that for an SSP of 10 Gyr, the metallic indices Mgb, Mg_2, and <Fe> are in fact weaker than their solar-scaled counterparts. It is also shown that the H β indices are stronger in the [α/Fe] enhanced SSP, a result of the hotter temperatures of the input stellar tracks. Nevertheless, the effect of [α/Fe] enhancement on stellar evolutionary tracks is negligible compared to the effect on the stellar atmosphere.

To create SSP models with varying alpha ratios, the [α/Fe] abundance as well as the fundamental stellar parameters (FSPs), $T_{\rm eff}$, log g, [Fe/H], must first be estimated from the observed stellar spectra. The derivation of FSPs is a complex process that requires self-consistency, and using FSPs from various compilations employing different techniques can introduce systematic errors and provide inconsistent results. Few FSPs have been reported in the literature for the MaStar spectral library stars prior to our own comprehensive derivations (Chen et al. in preparation; Lazarz et al. in preparation; Chen et al. 2020; Imig et al. 2022). Furthermore, we present the FSPs using solar-scaled [α/Fe] models in Hill et al. (2022, hereafter H22).

The task of estimating [α/Fe] for large catalogues of individual stellar spectra has been approached in several ways within the literature. The SEGUE Stellar Parameter Pipeline (SSPP) employ a χ^2 minimization approach using a grid of synthetic spectra and focus on a narrow wavelength range (4500–5500 Å) that is sensitive to [α/Fe] (Yanny et al. 2009; Lee et al. 2011). The spectral fitting is performed at the BOSS instrumental of $R \sim 2000$, similar to that of the MaNGA instrument employed in MaStar. SSPP apply weights to each α sensitive line within the wavelength window and calculate the averaged ratio. This approach is different to what is described for the FSPs in SEGUE (Lee et al. 2008a,b), where they use an array of techniques in different wavelength regions to obtain an average estimate of $T_{\rm eff}$, log g, and [Fe/H].

The APOGEE Stellar Parameter and Chemical Abundance Pipeline (ASPCAP; García Pérez et al. 2016) also uses χ^2 minimization and synthetic stellar spectra to estimate [α/Fe], but at a much higher spectral resolution ($R = 22\,500$) and a limited wavelength range (1.51–1.70 μm) compared to MaStar. Initially, all stellar parameters including some abundances such as [α/Fe], as well as microturbulence and rotational velocity, are fit with their optimization code FERRE. After this initial fit, the analysis is repeated for individual abundances in wavelength ranges that are sensitive to the abundance being measured (Jönsson et al. 2020).

There are also more data-driven techniques to estimate [α/Fe]. For example, in Imig et al. (2022), the authors estimate the FSPs as well as [α/Fe] and microturbulent velocity using a neural network approach. They train their model on MaStar spectra that have corresponding ASPCAP values and supplement this with hot theoretical spectra from Allende Prieto et al. (2018). The generative model created by the neural network is then used to fit MaStar spectra using χ^2 minimization.

In this paper, we present an independent measurement of [α/Fe] for MaStar, using two catalogues of synthetic stellar spectra and the Markov Chain Monte Carlo (MCMC) algorithm to estimate atmospheric parameters. In section 2, we outline the stellar spectral data and the synthetic model atmospheres used to derive atmospheric parameters. Section 3 describes the pre-processing required before analysis and briefly outlines the method used to estimate $T_{\rm eff}$, log g, [Fe/H], and [α/Fe]. As this is fully described in H22, we only highlight here the key points. Section 4 describes the results and concluding statements are made in Section 5.

2 DATA

2.1 Observations

Observations for the MaNGA Stellar Library (MaStar) were carried out using the 2.5 m Sloan Foundation Telescope (Gunn et al. 2006) at the Apache Point Observatory. The survey was designed to collect empirical stellar spectra that can be used to model galaxy observations from the Mapping Nearby Galaxies at Apache Point Observatory (MaNGA) survey (Bundy et al. 2015; Drory et al. 2015; Law et al. 2015, 2016; Yan et al. 2016a,b; Blanton et al. 2017). With this in mind, the MaStar observations were taken with MaNGA fibre bundles and BOSS spectrographs. The benefit of this is that MaStar spectra have the same wavelength coverage as MaNGA IFU data (3620–10350 Å) with a wavelength-dependent spectral resolution of $R \sim 1800$. Furthermore, accurate flux calibration and high signal to noise (S/N) per object (median = 96 per spectral pixel) was achieved by using the fibre bundles. As a result of this, the MaStar spectra have been used for emission-line measurements in the MaNGA data analysis pipeline (Abdurro'uf et al. 2022).

In order to create robust stellar population models, MaStar has observed stars spanning the stellar parameter space of $T_{\rm eff}$, log g, [Fe/H], and [α/Fe]. As a result, population models using MaStar spectra are ideal for modelling the SED of MaNGA galaxies (Neumann et al. 2022), globular clusters (Maraston et al. 2020), and simulated galaxy spectra (Nanni et al. 2022) for the purpose of evolutionary population synthesis. Further details regarding the observing strategy, instrumental set-up and resolution of MaStar can be found in Yan et al. (2019) and Law et al. (2021).

As in H22, we analyse all 59 266 high-quality spectra for 24 290 stars in MaStar (Yan et al. 2019), which uses the `mastar-`

goodspec file. All MaStar data are now publicly available and described in Abdurro'uf et al. (2022). Along with the release of MaStar spectra is the value added catalogue of stellar parameters from the studies that have estimated parameters in parallel (Chen et al. in preparation; Lazarz et al. in preparation; Hill et al. 2022; Imig et al. 2022) and a median calibrated catalogue which combines the parameters from the individual catalogues, including the parameters presented here. A comprehensive comparison between these catalogues of stellar parameters will be made in a future publication (Yan et al. in preparation). The parameters described in this paper are an update from those presented in the value-added catalogue and will be different due to the inclusion of [α/Fe] and minor updates to our parameter pipeline.[1]

In addition to the individual observations, we also analyse the uniform resolution, stacked spectra. As the resolution varies between each observation, spectra have been unified in terms of their resolution curves and split into four percentiles that allows one to select the spectra with the highest resolution at each wavelength. With unified resolution, multiple visits of the same star can be combined to produce a single spectrum of higher S/N. In this work, we also analyse the 60th percentile resolution curve for stacked visit spectra, which contains 5106 spectra and has a median S/N of 119. Further details of the uniform-resolution spectra can be found in Abdurro'uf et al. (2022) and in the SDSS DR17 online documentation.[2]

2.2 Models

We perform the full spectral fit using the synthetic spectra from model atmospheres of MARCS (Gustafsson et al. 2008) and BOSZ-ATLAS9 (Mészáros et al. 2012; Bohlin et al. 2017). Synthetic model atmospheres are opted for again due to the wide coverage in parameter space and high resolution that can be matched to observations. We match the resolution of the model spectra to the wavelength dependent resolution of MaStar using a Gaussian kernel. The spectra are then resampled to the velocity sampling of SDSS spectrographs (69 $\mathrm{km\,s^{-1}\,pixel^{-1}}$).

The model grid coverage for $T_{\rm eff}$, log g, [Fe/H] is shown in fig. 3 of H22, which remains unchanged for BOSZ-ATLAS9 and varies depending on [α/Fe] for MARCS. The BOSZ-ATLAS9 models provide spectra at [α/Fe] = −0.25, 0, 0.25, and 0.50 for all combinations of $T_{\rm eff}$, log g, and [Fe/H]. The MARCS models provide spectra at [α/Fe] = −0.40, 0, and 0.40; however, these are not available for all parameter combinations. For $-2 <$ [Fe/H] $<$ 1, all [α/Fe] combinations are available. For $-2.5 <$ [Fe/H] < -2, only the solar scaled and enhanced models are available ([α/Fe] = 0, 0.4). Furthermore, we fix the microturbulence parameter to 2 $\mathrm{km\,s^{-1}}$ and do not account for rotational velocity ($v \sin i$). In H22, we show that at the resolution of MaStar, the effect of line broadening from $v \sin i$ is negligible up to 200 $\mathrm{km\,s^{-1}}$. However, we cannot rule out that MaStar does not contain stars with $v \sin i > 200$ $\mathrm{km\,s^{-1}}$ and therefore suggest that the parameters of the very hottest stars, where fast rotators are more likely to exist, are used with care. The determination of $v \sin i$ for MaStar spectra is the subject of future work. Using LAMOST spectra of hot stars at a similar resolution to MaStar, Xiang et al. (2022) demonstrate that the determination of $v \sin i$ for spectra with S/N ∼100 can be theoretically determined with a precision of 10 $\mathrm{km\,s^{-1}}$.

To see how the synthetic spectra of MARCS and BOSZ-ATLAS9 react to changes in [α/Fe], we fix $T_{\rm eff}$, log g and [Fe/H] while varying [α/Fe] and focus on a few sensitive absorption lines. In Fig. 1, we show synthetic model spectra for MARCS (top row) and BOSZ-ATLAS9 (bottom row), fixing $T_{\rm eff} = 5000$ K, log $g = 4$, and [Fe/H] = 0, while varying [α/Fe] = −0.25, 0.0, 0.4. The spectra have been interpolated where necessary in order to make a fair comparison. Furthermore, each spectrum is normalized by dividing by the median flux; therefore, differences in the continuum between MARCS and BOSZ-ATLAS9 will mean that their relative position on the y-axis may differ.

The most prominent features shown in the left-hand panels are the lines of Mg_b in the range of 5160–5190 Å; as [α/Fe] is increased, we see deeper absorption features as expected. In the centre panels, we show the lines of Co I at 5647 and Fe I at 5661–5662 Å. The right-hand panels show the same spectra but focuses on the first two lines of the Ca II triplet at 8498 and 8542 Å. The comparison here between the two models show similar spectral features between the two model libraries that behave in a similar way as [α/Fe] is adjusted.

3 METHOD

The full spectral fitting routine described in H22 is used again for this analysis for completeness we briefly describe the key features with the addition of [α/Fe] as a fourth free parameter.

Before analysis MaStar spectra are corrected for galactic extinction with $E(B-V)$ values from the 3D dust map of Green et al. (2019). Since H22, we have cross-matched MaStar observations with *Gaia* EDR3 (Gaia Collaboration 2021) that returns valid parallax and photometry estimates for 99 per cent of the 24 290 stars in the MaStar goodspec file. As the dust map values are based on *Gaia* DR2 distances, the updated distances from Bailer-Jones et al. (2021), which use *Gaia* EDR3 parallax values, were used to sample more accurate extinction values. Further details of this procedure will be described in Yan et al. (in preparation).

Using photometry from the *Gaia* EDR3 cross-match, we create a CMD of MaStar observations and overplot the PARSEC theoretical isochrone tracks from Bressan et al. (2012) for ages 2 Myr to 10 Gyr. Around each observation a box is created in *Gaia* colours of size $\Delta(G_{\rm BP} - G_{\rm RP}) = 0.8$ and magnitude $\Delta(M_G) = 2$, the minimum and maximum values for $T_{\rm eff}$ and log g for the isochrones passing through each box are recorded and used for the flat priors in the MCMC routine. No priors are used for [Fe/H] and [α/Fe].

We use an MCMC approach to map the parameter space of the four atmospheric parameters: $T_{\rm eff}$, log g, [Fe/H], and [α/Fe]. The starting values of the MCMC walkers are randomly sampled from a uniform distribution within the limits of the priors. In the case of [Fe/H] and [α/Fe], starting values are sampled within the grid limits. As each combination of parameters are proposed by the MCMC chains, they are used to create a linearly interpolated model spectrum which is convolved with the observed spectrum before being used in the likelihood function. The convolution uses the penalized pixel fitting routine (PPXF; Cappellari & Emsellem 2004; Cappellari 2017) and involves fitting the spectrum with sixth-degree multiplicative polynomials. This convolution is done to fit the spectral continuum and can account for small velocity offsets in the observations. By doing the convolution 'on-the-fly', we avoid having to create convolved model spectra for each observation.

[1]Stellar parameters from all studies can be found at https://data.sdss.org/sas/dr17/manga/spectro/mastar/v3_1_1/v1_7_7/vac/parameters/v2/. The solar-scaled [α/Fe] parameters presented in H22 and the parameters presented here can also be found at https://www.icg.port.ac.uk/mastar/.
[2]https://www.sdss.org/dr17/mastar/mastar-spectra/

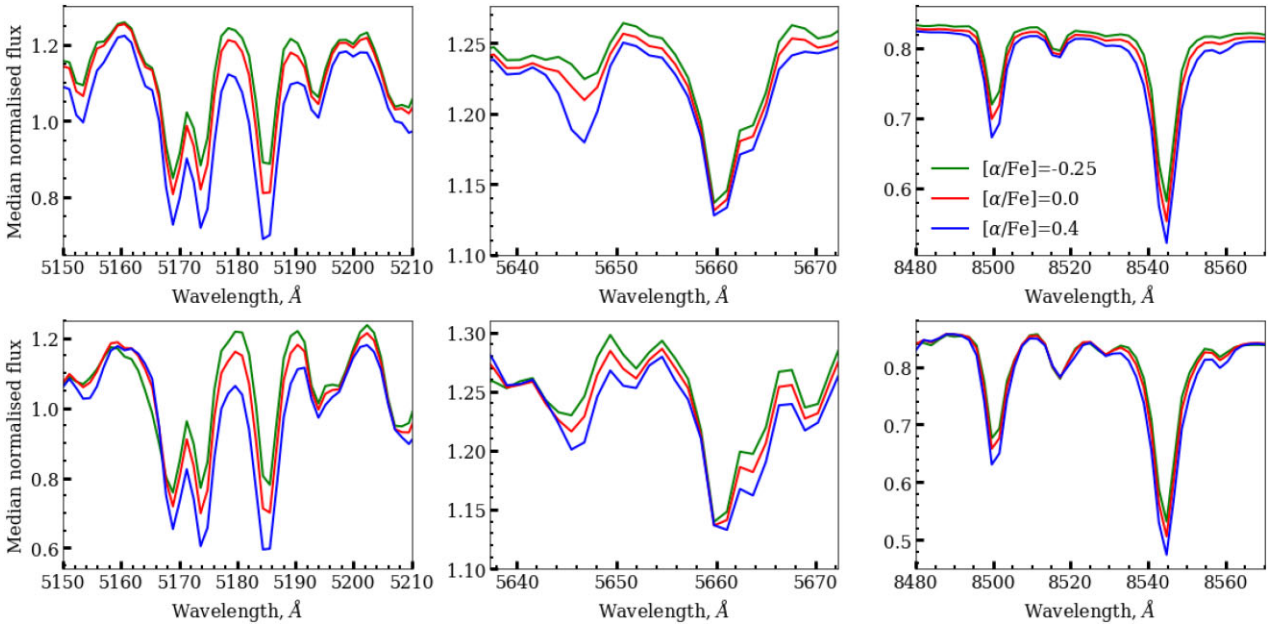

Figure 1. *Top row*: [α/Fe] sensitive features for MARCS synthetic spectra with $T_{\rm eff} = 5000$ K, log $g = 4$ and [Fe/H] $= 0$. We vary [α/Fe] between -0.25 and 0.4 as to cover the intersecting range between both model libraries. *Left*: Absorption lines of Mg$_b$ in the range of 5160–5190 Å. *Centre*: Co I at 5647 Å and Fe I at 5661–5662 Å. *Right*: Ca II at 8498 and 8542 Å. *Bottom row*: Same as above but for BOSZ-ATLAS9 models.

The log-likelihood function is used to map the posterior distribution for each of the four parameters. The parameters $T_{\rm eff}$ and log g are estimated using the median value of the posterior as these incorporate the priors and will reflect the prior estimate if no strong solution is found. For [Fe/H] and [α/Fe], each parameter is estimated using the maximum of the posterior distribution (i.e. the maximum a posteriori). With the estimated parameters, a new interpolated model is generated and the χ^2 statistic calculated for the purpose of cleaning the final catalogue. The analysis is done for BOSZ-ATLAS9 and MARCS models independently[3] and the parameters selected are based on the lowest χ^2 values.

3.1 Convergence and quality assessment cuts

In H22, we estimate the atmospheric parameters using an implementation of the affine invariant ensemble sampler (Goodman & Weare 2010) provided in the Python package EMCEE (Foreman-Mackey et al. 2013). The posterior distribution was previously generated using 40 walkers and 2000 iterations, 200 of which are discarded as a burn-in phase. For the estimation of the parameters presented in H22, such a set-up was adequate and any bad fits or non-physical parameter combinations were removed through our quality cuts using the χ^2 statistic measured from the observation and polynomial corrected model with the estimated parameters from the spectral fitting procedure. However, the determination of [α/Fe] is more delicate due to subtle variations in only a few lines within our wavelength range driving the movement of walkers to a solution. We now impose an additional quality check by calculating the integrated autocorrelation time (IAT) every 50 steps after the burn-in period, which is still set at 200 iterations. The IAT is a diagnostic used to measure the effective number of independent samples and can indicate if chains have converged. In Foreman-Mackey et al. (2013), they suggest running the sampler for 10 times the IAT, at which point the walkers should be sufficiently independent. To ensure a robust estimation of parameters, we consider the sampler converged when the number of iterations exceeds 15 times the IAT for each parameter and if the parameters have changed by less than 1 per cent from the last 50 iterations.

To see the relation of the IAT with S/N and to gauge how many iterations we may expect for convergence, we performed a test whereby all spectra were run for 1800 iterations with 40 walkers. After calculating the chains, the IAT was calculated for each spectrum and for each parameter, then plotted as a function of S/N (see Fig. 2). All panels show the IAT for [α/Fe], the left shows this relation coloured by the estimated $T_{\rm eff}$ and the middle panel by log g. The right panel shows where the highest density of points reside in this distribution. For the majority of spectra, as the S/N increases, the IAT decreases which indicates faster convergence of the MCMC chains. Conversely, for spectra of giant stars, the S/N has no constraint on the convergence of the chains. We expect this is due to the deep molecular bands in these spectra which are not trivial to match with synthetic atmospheres. We also see that the highest IATs are approximately 200 and that this is similar across all parameters. Given that in our analysis we impose a limit of 15 times the IAT, then we require at least 3000 iterations to ensure sufficient time for all chains to be independent and converged. This number of iterations was arrived at by multiplying the maximum IAT of $\sim$200 from the test by 15, the limit of IATs we define.

Due to the additional step of calculating a polynomial corrected model using pPXF in our log probability function, the analysis of each spectrum is already relatively slow and requires a maximum limit of iterations, regardless of whether it has reached the IAT criteria. We set the maximum iterations to 5000 and find that only 1.5 per cent of spectra were unable to converge within this limit. The parameters for such instances are flagged as invalid and are not included in the final catalogue. The median number of iterations required for the IAT criteria and for the parame-

[3]MARCS models are only used when the prior on $T_{\rm eff}$ is below 5000K as the BOSZ-ATLAS9 models provide better fits at higher temperatures.

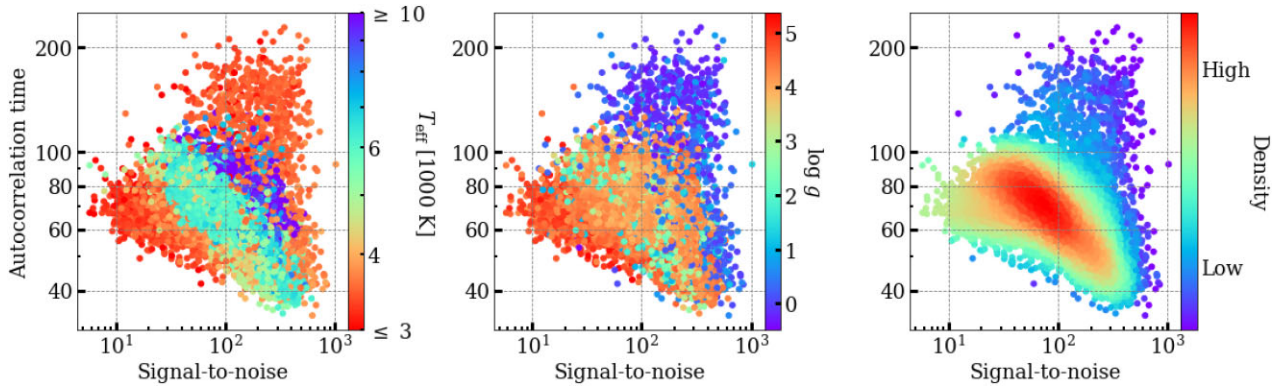

Figure 2. The integrated autocorrelation time calculated after 1800 iterations for [α/Fe], as a function of the S/N for each spectrum. From left to right, plots are coloured by $T_{\rm eff}$, log g, and the density of points, where red represents the highest density.

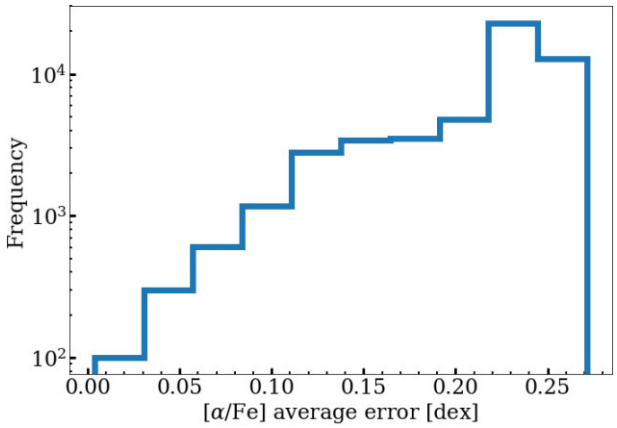

Figure 3. Distribution of the averaged upper and lower bound errors for spectra with valid FSPs.

ters to change less than 1 per cent within 50 consecutive iterations is 700 and 950 for MARCS and BOSZ-ATLAS9 models, respectively.

In addition to the convergence criteria, we also flag spectra as invalid based on the error of [α/Fe] once the sampler has converged. In Fig. 3, we show the distribution of the average of the error interval (upper bound and lower bound on the error) for [α/Fe]. As shown, there is a significant increase in the number of spectra with an error greater than 0.22 dex, which are mainly attributed to metal poor main sequence stars for which it is not trivial to determine their [α/Fe]. Consequently, we include only parameters that have an average error less than 0.22 dex in our quality measure. We apply this as a separate flag for the [α/Fe] values only.

The conditions for valid parameters described in H22 are also used in combination with the aforementioned criteria. Namely, we flag spectra based on the χ^2 fit between the model with the selected parameters and observation. Spectra with $\chi^2 > 30$ are flagged as invalid, except when $T_{\rm eff} < 4000$ K. We allow for poor fits at low temperatures to allow for the complex features, such as TiO bands and stellar flares, found at such temperatures and the shortcomings of theoretical atmospheres in this domain.

4 RESULTS

We firstly present the spectroscopic Hertzsprung–Russel diagram (HRD) to see how including [α/Fe] affects the FSPs and then make a comparison with literature values of [α/Fe]. The sky distribution of [α/Fe] is then shown and the relationship between [Fe/H] and [α/Fe] is plotted. We also test how robust our measurement of [α/Fe] is to changes in S/N. Finally, we explore how our results are restricted by the chemical evolution of the MW and probe how these measurements may be used to create SSP models of varying [α/Fe].

4.1 The fundamental stellar parameters

In Fig. 4, we show the spectroscopic HRD for our latest FSPs that have been derived in parallel with [α/Fe]. Since our constraint on valid values of [α/Fe] removes most spectra with $T_{\rm eff} > 10\,000$ K, we show the valid parameters that may be used for $T_{\rm eff}$, log g, and [Fe/H] only. In Table 1, we show the errors for the subset of spectra represented in the HRD, which are separated by their temperature: $T_{\rm eff} < 5000$, $5000 \leq T_{\rm eff} < 15\ 000$, and $T_{\rm eff} \geq 15\,000$ K. For each $T_{\rm eff}$ interval shown in the table, the errors are calculated based on the median value from the posterior distribution function (PDF) of each spectrum and from the median of the repeat observations of the same star (repeat observations). The repeat observation errors are based on 15 345 stars, represented by 50 321 spectra, as 8945 stars only have one observation. The results show that for all parameters, except for log g, the median error generally increases with $T_{\rm eff}$. Unlike the cut we impose on the error of [α/Fe] to remove unreliable parameters, we have decided not to apply this to [Fe/H] as its estimation is dependent on more lines than [α/Fe], especially as $T_{\rm eff}$ increases. Nevertheless, the estimation of [Fe/H] for hot stars is difficult as absorption lines become sparse. In the table, we also show the errors for [α/Fe]; however, these are based on the smaller subset of spectra using the additional cleaning criteria for [α/Fe] described in Section 3.1.

We compare these values to the case with solar-scaled [α/Fe] in order to see what effect including [α/Fe] has on the overall parameter distribution. A summary of the statistics is shown in Table 2 and a direct comparison shown in Fig. 5. For $T_{\rm eff}$ there is a negligible difference at low and intermediate temperatures, with a preference towards hotter temperatures above ∼22 000 K when using solar-scaled models. No systematic offset is found for log g at any temperature. There is a general offset towards higher [Fe/H] when using solar scaled models, ranging from 0.14 dex for $T_{\rm eff} < 5000$ K to 0.06 dex for $T_{\rm eff} \geq 15\,000$ K. In terms of the standard deviation (σ), the scatter at low and intermediate temperatures is small, increasing to 869 K in the hottest bin. There is

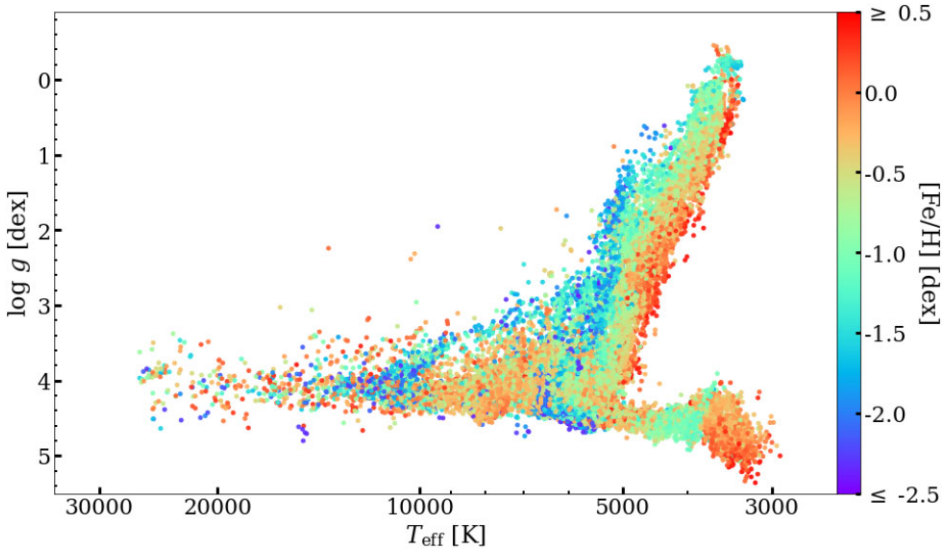

Figure 4. Spectroscopic HR diagram showing the distribution of parameters after the χ^2 quality cut, coloured by the metallicity.

Table 1. Median errors for each atmospheric parameter. Errors are split into low, medium, and high temperature bins and are estimated two ways. Error source 'PDF' represents the errors calculated from the posterior generated by the walkers of the MCMC and 'Repeat observation' are calculated by taking the standard error of repeat observations.

FSP	Error source	$T_{\rm eff}$ < 5000	5000 ≤ $T_{\rm eff}$ <15 000	$T_{\rm eff}$ ≥ 15 000
$T_{\rm eff}$	PDF	181	408	2614
	Repeat observations	17	33	273
log g	PDF	0.41	0.37	0.38
	Repeat observations	0.03	0.03	0.04
[Fe/H]	PDF	0.38	0.56	0.89
	Repeat observations	0.06	0.10	0.42
[α/Fe]	PDF	0.13	0.18	0.21
	Repeat observations	0.03	0.03	–

Table 2. Median differences and standard deviation (σ) between FSPs when using solar-scaled model atmosphere and when allowing for a variable [α/Fe]. The comparison is made in three temperature bins, as shown. Temperatures are shown in units of Kelvin.

FSP	$T_{\rm eff}$ < 5000		5000 ≤ $T_{\rm eff}$ <15 000		$T_{\rm eff}$ ≥ 15 000	
	Median difference	σ	Median difference	σ	Median difference	σ
$T_{\rm eff}$	5	48	5	72	88	869
log g	0.00	0.09	0.00	0.05	0.01	0.06
[Fe/H]	0.14	0.24	0.08	0.29	0.06	0.86

a small scatter for log g with little dependence on $T_{\rm eff}$. The standard deviation for [Fe/H] increases with $T_{\rm eff}$ and as shown in Fig. 5, with decreasing [Fe/H]. This is unsurprising since hot stars have less lines to constrain [Fe/H] and these become weaker with decreasing [Fe/H].

4.2 [α/Fe]

4.2.1 Literature comparison

In order to assess the accuracy of our estimated [α/Fe] it is useful to compare to other parameter catalogues. Doing so, we are able to identify degeneracies in our parameter estimation which we can calibrate for if necessary. First, we compare to the output of ASPCAP, the parameter pipeline for the APOGEE survey. The cross-match with our spectra, applying the strict [α/Fe] flag, returns 3148 spectra for 1420 stars. As ASPCAP analyses spectra at a resolution almost ten times greater than MaStar we would expect their values of elemental abundances to be more accurate.

In the top panel of Fig. 6, we show the comparison of [α/Fe] with ASPCAP. The y-axis shows our value of [α/Fe] minus ASPCAP's and the colour shows log g as estimated by ASPCAP. At the hottest temperature, which are populated by dwarfs and subgiants, there is good agreement with no systematic difference. The difference in [α/Fe], Δ[α/Fe], of the coolest dwarf stars at $T_{\rm eff}$ 3300–3500 K is also in agreement. There is a clear trend in Δ[α/Fe] for warmer dwarf stars (log g > 4), where the discrepancy peaks at ∼4000 K and reduces for increasing $T_{\rm eff}$; this is further investigated in Appendix A. Overall, we find a standard deviation of 0.14 dex with a median offset of 0.01 dex. Although the median difference is negligible, it is clear that there are noticeable discrepancies for certain stellar types and that these offsets cancel out when considering the overall distribution.

We also compare our [α/Fe] values with those of Imig et al. (2022). Once applying the quality cuts to our parameters and those from Imig we find a cross-match of 16 726 spectra for 9008 stars. The comparison is shown in the middle panel of Fig. 6 with the same format as with ASPCAP. From this, we see significant scatter that is dependent on $T_{\rm eff}$ and log g. The difference is centred about zero for intermediate temperatures (5000–5500 K), but increases with $T_{\rm eff}$ where we estimate higher [α/Fe] than Imig et al. (2022). At lower temperatures there is no clear trend except for that we generally estimate a higher value of [α/Fe]. In summary, the median offset between our results and that of Imig et al. (2022) is 0.08 dex with a standard deviation of 0.16 dex.

Finally, we compare our [α/Fe] values to those reported by *Gaia* DR3 (Creevey et al. 2022; Fouesneau et al. 2022), which were

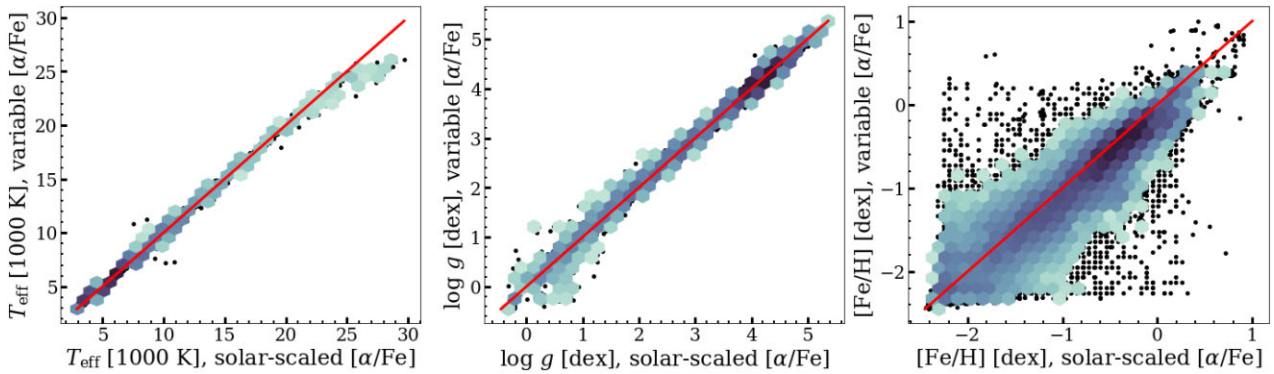

Figure 5. Comparison between $T_{\rm eff}$, log g, [Fe/H] when using solar-scaled [α/Fe] model atmospheres and allowing for a variable [α/Fe]. The dark colour hexagons represent denser regions, black data points are individual spectra and the red diagonal line represents the one-to-one relationship.

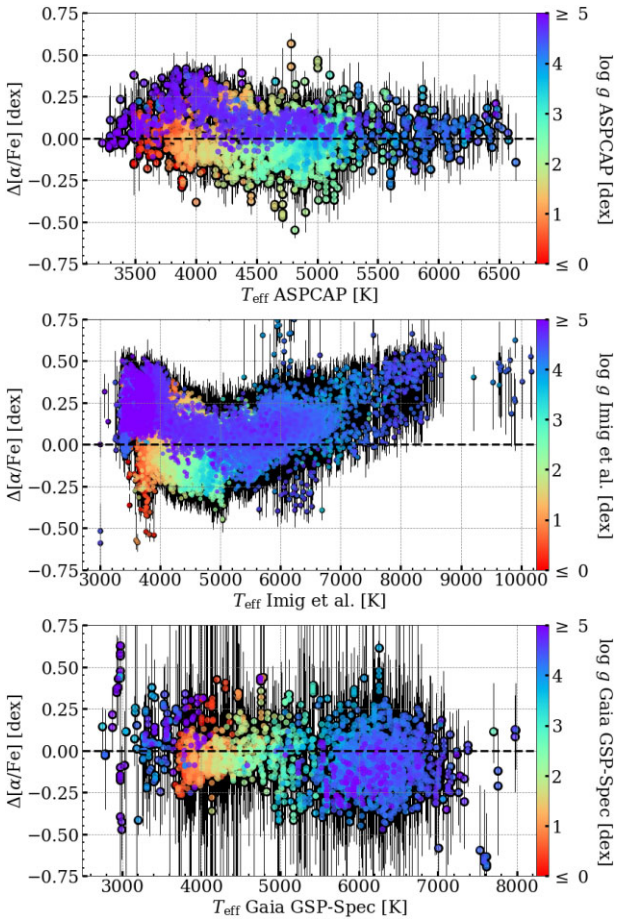

Figure 6. *Top*: The difference between our [α/Fe] minus ASPCAP's as a function of ASPCAP $T_{\rm eff}$, also coloured by their log g. Errors from both catalogues have been combined in quadrature and are shown by the black error bars. *Middle*: The same as above, but comparing to the [α/Fe] values of Imig et al. (2022) (our value minus theirs). Note that the x-axis scale is different to the above. *Bottom*: The comparison of [α/Fe] using values from *Gaia* GSP-Spec (Creevey et al. 2022; Fouesneau et al. 2022), in the same format as above.

calculated using the General Stellar Parametrizer from spectroscopy (GSP-Spec) algorithm. Specifically, we compare to the Matisse-Gauguin output of GSP-Spec, as this provides the largest crossmatch of spectra once quality flags are accounted for, resulting in 2892 matches. This offers another unique comparison as these stellar parameters have been calculated at $R \sim 11\,500$ in the wavelength range 8450–8720 Å.

The lower panel of Fig. 6 shows the difference in [α/Fe] (our value minus *Gaia*) as a function of their $T_{\rm eff}$ and coloured by their estimated log g. Some errors for the *Gaia* [α/Fe] are significant, causing error bars to go beyond the y-axis scale. We see that our values are fairly consistent for low and intermediate values of log g. The dispersion of points appears to increase at log $g \gtrsim 4$ and for $T_{\rm eff} \gtrsim 5000$ K. Unfortunately, there are not enough data points to conclude whether the trends seen for cool dwarfs in the above panels is consistent here. Overall we find a median offset of −0.07 dex and a standard deviation of 0.15 dex.

4.2.2 *[α/Fe] for galaxy evolution*

The relationship between [Fe/H] and [α/Fe], also known as the Tinsley–Wallerstein diagram, is shown in Fig. 7. Darker hexagons represent denser regions and single black points are outside of our minimum criterion to form a hexagon (2 data points). We apply the more conservative quality cut here, removing spectra with an average [α/Fe] error greater than 0.22 dex. We observe a well-defined negative correlation between [Fe/H] and [α/Fe] in agreement with our understanding of the chemical evolution of the MW. Additionally, there is a plateau at [Fe/H] < -1.0 dex formed from a combination of the model grid and by the enrichment of α peak elements caused by halo stars. We find a median value of 0.1 dex for [α/Fe] and −0.40 dex for [Fe/H]. When comparing the same stars with the results from ASPCAP, we find that their median metallicity is also below solar at −0.34 dex. This implies that we are either sampling a relatively metal-poor distribution of stars, or, as has been alluded to in the literature, the Sun formed in a different population of stars and has migrated to its current position from the inner disc. Further investigation of this is beyond the scope of this paper.

In Fig. 8, we show a sample of MaStar stars in galactic coordinates. The distances were calculated using parallax values from the Gaia crossmatch and used with the *Gaia* RA and Dec. for the sky position. Data points are coloured by our estimated value of [α/Fe], using the same quality cut to select spectra with reliable parameters – i.e. we are not showing the full sample of MaStar stars. Furthermore, as our estimate of [α/Fe] will vary from multiple observations due to random error, we present the average of these values. The left panel shows an edge-on view of the MW and a general shift in [α/Fe], moving from sub-solar to solar values in the disc and then becoming generally more enhanced towards the halo. This is in line with our

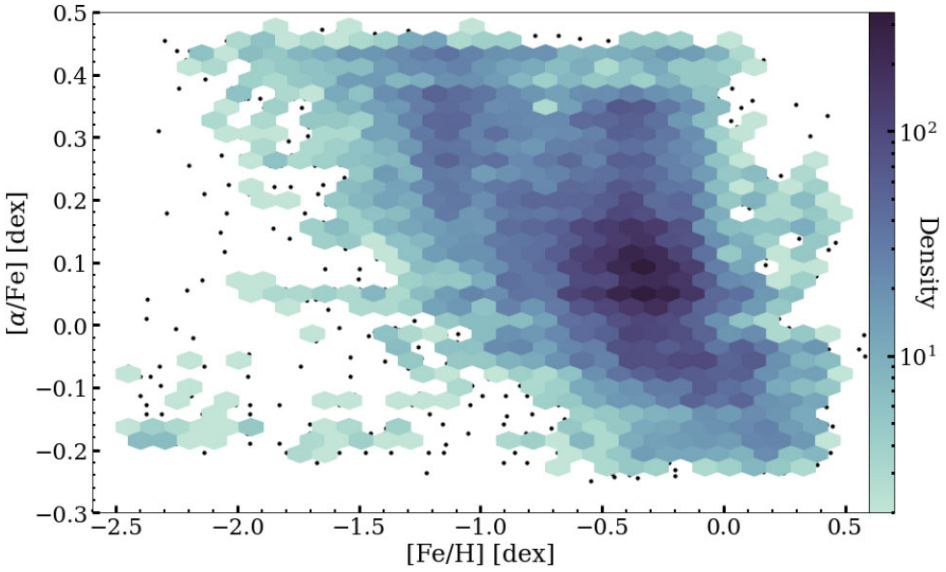

Figure 7. [Fe/H] versus [α/Fe] for the good visits spectra once the χ^2, IAT criteria and average [α/Fe] error cuts are applied, coloured by density.

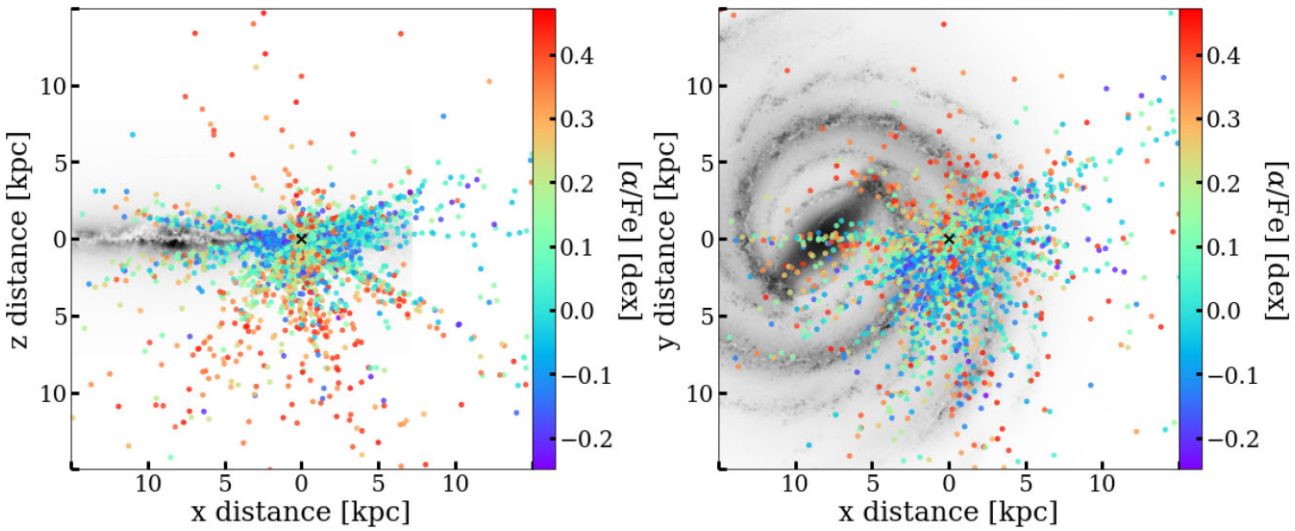

Figure 8. *Left*: An edge-on view of the MW shown in grey, with the sky distribution of a sample of MaStar stars in galactic coordinates. The distance to each star is shown in kiloparsecs (kpc) and each coloured by our estimated [α/Fe]. The stars shown are represented by those with a reliable estimate of [α/Fe], as described by our quality flags, and their average value of [α/Fe] is used where there are repeat observations. The position of the Sun is represented by the black cross in the centre of the panel. *Right*: The same as the left panel, but showing a face-on view of the MW. Background images of the MW were provided by NASA/JPL-Caltech/R. Hurt (SSC/Caltech) and ESA *Gaia* EDR3, respectively. The plots were created using the mw-plot PYTHON package: https://github.com/henrysky/milkyway_plot/.

understanding of the chemical abundance pattern of MW stars (e.g. Venn et al. 2004). Furthermore, in the right panel we show a face-on view of the MW with the same stars and their average [α/Fe] values. This provides an alternative view of their distribution in the MW.

4.3 Stacked and LSF homogenized spectra

To see how our parameter estimation changes when using the highest S/N spectra in MaStar we analyse the stacked, uniform resolution catalogue. As previously described, for each observation the spectra have been unified in terms of their resolution and split into four percentiles. Doing so allows one to stack the spectra, increasing their S/N. For this analysis we use the 60th percentile curve, representing the highest resolution at each wavelength. These are also useful for SSP models based on a homogeneous set of spectra leading to a better spectral resolution. The same MCMC routine was applied to the 5106 stacked spectra and the α cut applied, recovering 1678 valid spectra parameters.

In Fig. 9, we show comparison model fits for an example main sequence star, the estimated parameters of which are stated in the caption. Single observations and their respective model fits are shown in the top panel, with the stacked spectrum and model fit shown in the bottom panel. The average S/N for the single observation spectra is 62 and the S/N for the stacked spectrum is 104. This enhancement in signal is evident at all wavelengths, but particularly noticeable at either end of the spectrum. A similar comparison is made for a cooler

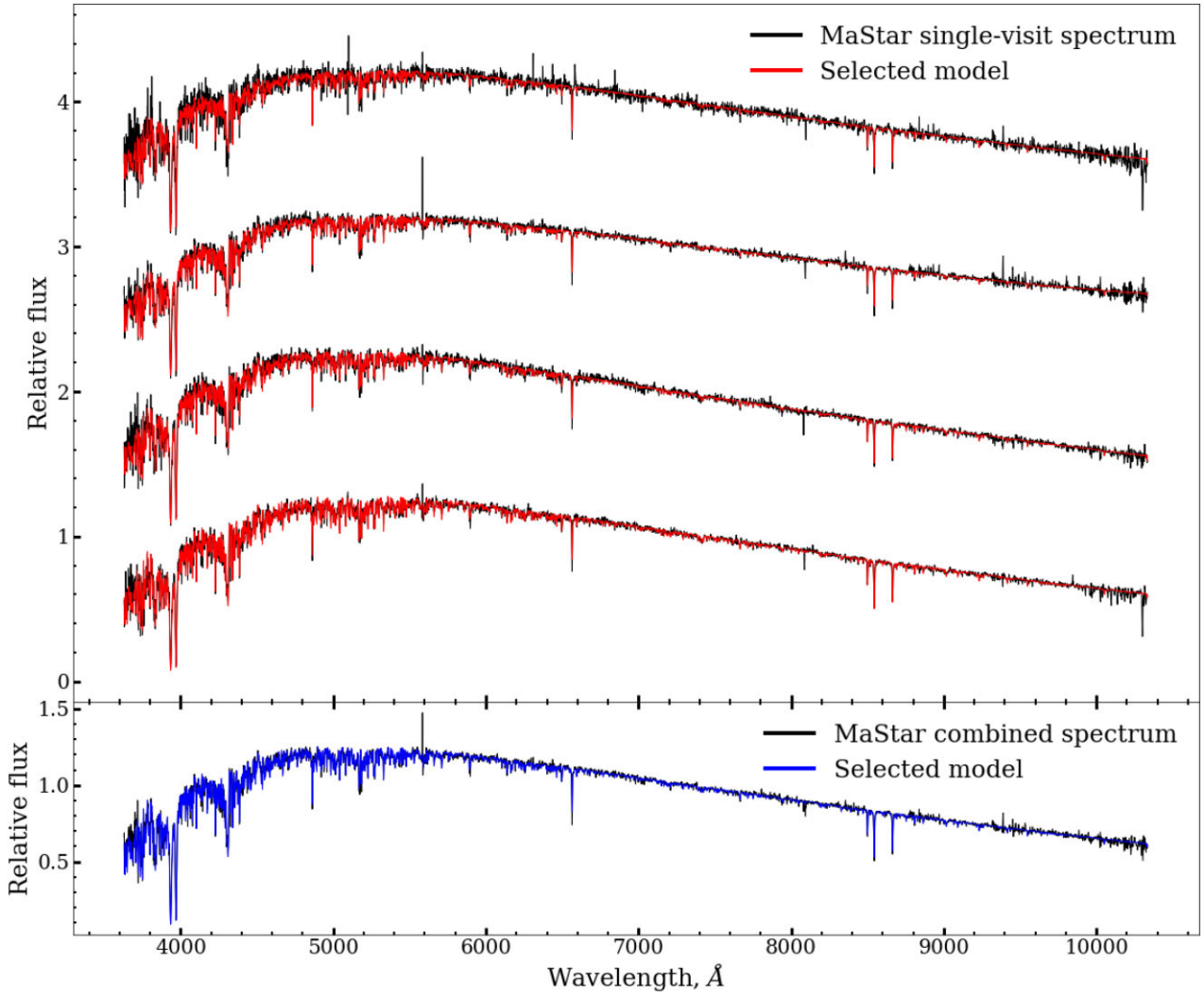

Figure 9. *Top panel*: Single visit spectra (black) for MaNGA ID 3-1570928314 and their selected model spectra (red). *Bottom panel*: The equivalent stacked spectrum (black) for the same star, with the selected model spectrum (blue). All model spectra are from BOSZ-ATLAS9 synthetics model atmospheres. The atmospheric parameters using the stacked spectrum are: $T_{\rm eff} = 5173$ K, log $g = 3.1$, [Fe/H] $= -1.0$ and [α/Fe] $= 0.2$. From top to bottom, single visit spectra represent a S/N of 40, 76, 57, and 76. The combined spectrum in the lower panel has a S/N of 104.

star with lower gravity in Fig. 10. Here, we see greater variance in the blue portion of the individual visit spectra and the spectral features become better defined once combining observations. The average S/N of the individual spectra is 81, using the stacked spectrum this improves significantly to 207. Furthermore, with better signal, we should be able to constrain the atmospheric parameters with greater accuracy. To test this, we take the average error for each parameter (average of the upper and lower error bounds), for each goodvisit spectrum, and calculate the median value for each set of errors. The median of the errors is then compared to the corresponding errors for the stacked visit stars. Doing so, we find a modest increase in accuracy for all parameters: $T_{\rm eff}$ improves by 81 K, log g by 0.02 dex, [Fe/H] by 0.11 dex and [α/Fe] by 0.01 dex. Consequently, there are clear advantages of using such enhanced signal spectra when developing simple stellar population models.

Fig. 11 shows a one-to-one comparison for $T_{\rm eff}$, log g, [Fe/H], and [α/Fe] using the goodvisits individual and stacked spectra, coloured by parameters from the stacked visit results. Stacked spectra results are repeated since there are multiple goodvisits spectra for every stacked one. Within each subplot is a histogram showing the goodvisits minus the combined spectra values. $T_{\rm eff}$ and log g show little to no scatter, with standard deviations of 42 K and 0.12 dex, respectively. The best agreement for log g is seen at intermediate values. For [Fe/H], a standard deviation of 0.12 dex is measured overall. For [α/Fe], most scatter is found in the range $0.2 - 0.4$ dex which is populated by the cool stars with log $g > 4.0$ discussed previously. The overall standard deviation is 0.07 dex, but increases up to 0.09 dex for [α/Fe] >0.2. Comparing these standard deviation values to the median errors measured for individual spectra in Table 1 gives a sense of the accuracy of our error estimates – noting that the spectra in the combined visit comparison are in the approximate range of $3000 < T_{\rm eff} < 10\,000$ K. For $T_{\rm eff}$, log g, [Fe/H], the error estimate from comparing goodvisits and combined spectra estimates returns errors lower than those estimated from the posterior and slightly larger than from repeat observations. A similar trend is seen for [α/Fe]; however, the error from the repeat observations is in the range $5000 \leq T_{\rm eff} < 15\,000$ K is consistent with the error measured from the combined visit comparison.

To further check whether our estimation of [α/Fe] is robust against changes in S/N, we make the same comparison with ASPCAP as was

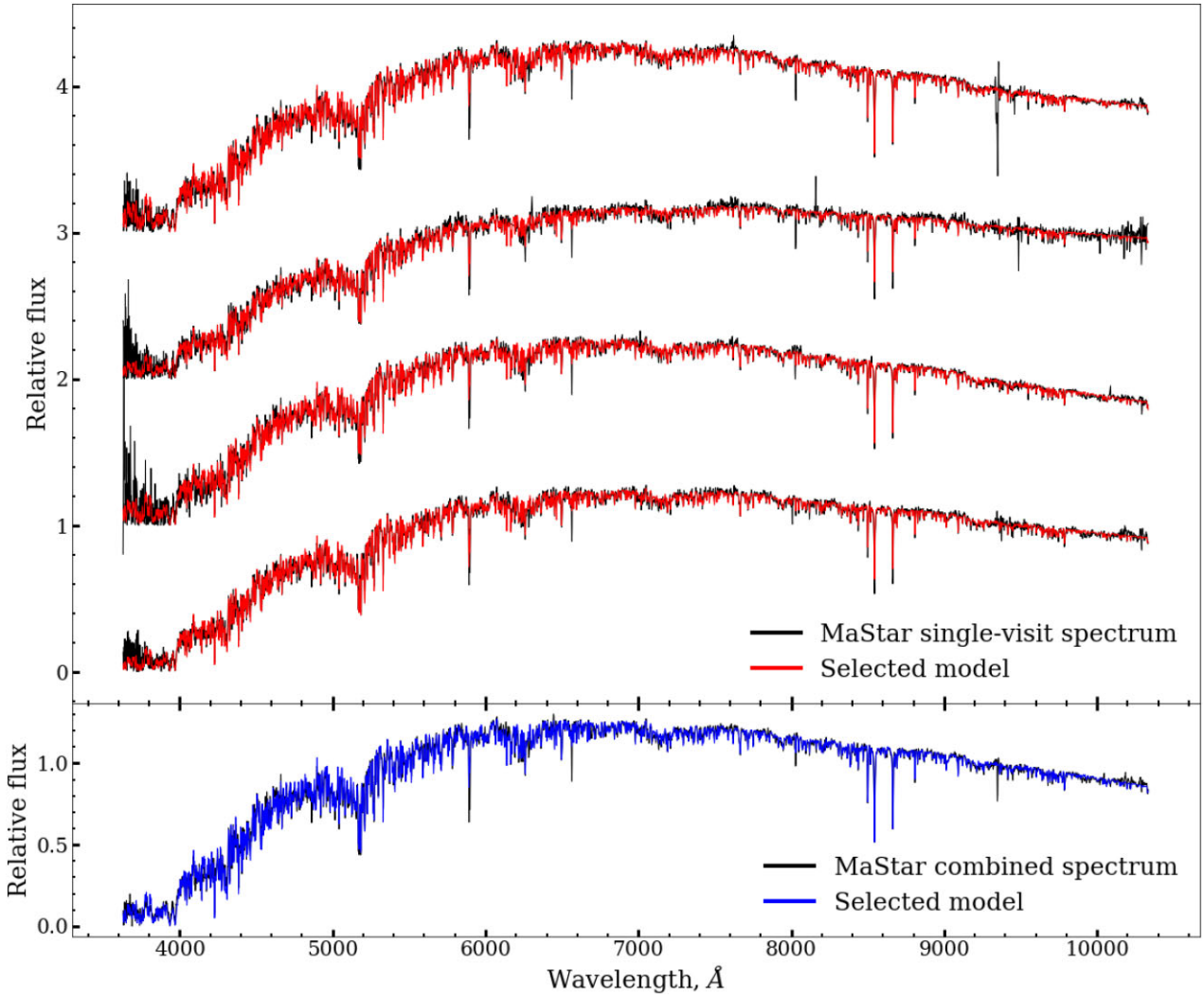

Figure 10. Same as Fig. 9 for MaNGA ID 3-125307389. The atmospheric parameters using the stacked spectrum are $T_{\rm eff} = 4052$ K, log $g = 1.3$, [Fe/H] $= -0.6$, and [α/Fe] $= 0.3$. From top to bottom, single visit spectra represent an S/N of 65, 112, 45, and 124. The combined spectrum in the lower panel has an S/N of 207.

done in the previous section. The comparison with the stacked spectra is shown in Fig. 12 for 186 stars. Similar offsets that were seen with the single goodvisit spectra are also seen here. In particular, the trend in Δ [α/Fe] for log $g > 4.0$ is repeated. From this, we conclude that the robustness of our [α/Fe] measurement does not correlate with S/N, at least for S/N < 119.

4.4 The bias of the MW

By developing stellar population models from empirical stellar spectra only, compared to using synthetic stellar spectra, one is restricted by the chemical enrichment history of the MW. As we have seen from Fig. 7, sub-solar [Fe/H] SSP models can only be constructed at super-solar values of [α/Fe]. This α bias of the MW is what led Thomas, Maraston & Bender (2003) to adopt a semi-empirical approach for their model atmosphere calculations, generating super-solar [α/Fe] models differentially.

In Fig. 13, we plot HRDs showing the distribution of [α/Fe] for five intervals of [Fe/H]. The intervals are shown in the title of each panel and are based on those used to create stellar population models in Maraston et al. (2020). This shows that most stellar phases are covered in the range of $-1.5 <$ [Fe/H] ≤ 0.2. We note that there is a paucity of points at $T_{\rm eff} \sim 4000$ K, log $g \sim 4.5$, which is most evident in the $-0.2 <$ [Fe/H] ≤ 0.2 bin. We have thoroughly investigated this feature and suspect that it is a combination of factors. Firstly, we rule out the possibility that it is a problem with our parameter pipeline by fitting solar [Fe/H] model spectra for both MARCS and BOSZ-ATLAS9 in this $T_{\rm eff}$ and log g range; the input parameters are well recovered in this test. We then inspected the parameters of Chen et al. (in preparation) in this range, as they also use MARCS and BOSZ-ATLAS9 models, and find similar features. Below 4500 K, the majority of these spectra are fit with MARCS, rather than BOSZ-ATLAS9, which is based on the lower χ^2 of the model fit. In fact, when we take the BOSZ-ATLAS9 solution, the underdensity is reduced. We note that for $T_{\rm eff} < 4000$ K, line blanketing effects increase due to the synthesis of TiO and H_2O entering the stellar atmosphere models (Gustafsson et al. 2008). It is possible that these heavy molecules exist in our observed spectra at temperatures above this and we are seeing complications in modelling [Fe/H] when trying to fit spectra with models that do not account for enhanced blanketing effects above 4000 K. Lastly, we have used our crossmatch with Gaia photometry to see where

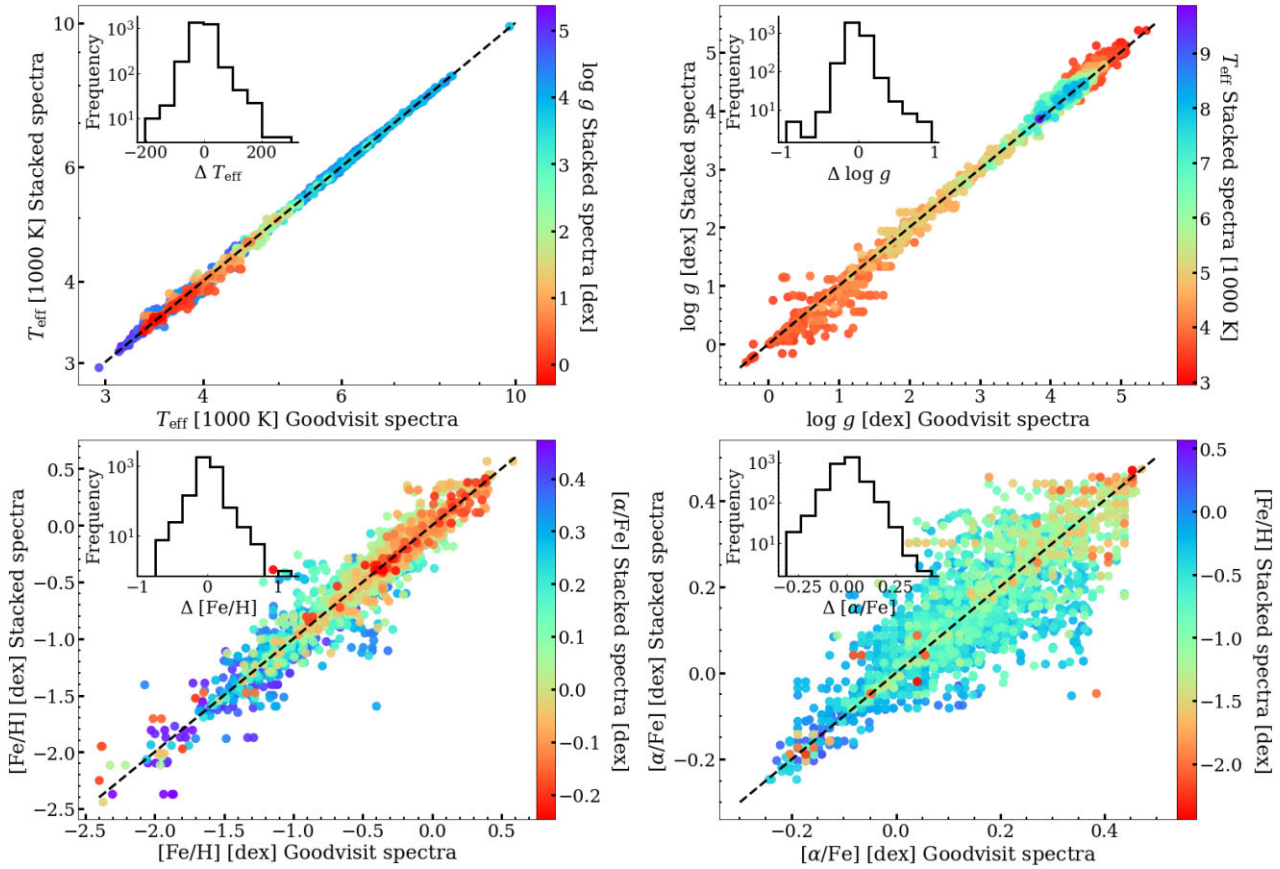

Figure 11. Comparison of $T_{\rm eff}$ (top left), log g (top right), [Fe/H] (lower left), and [α/Fe] (lower right) retrieved from fitting individual spectra from the goodvisits catalogue versus fitting the stacked spectra with increased S/N. Data points are coloured by parameters recovered from the stacked spectra. The dashed black line shows the one-to-one relation. Each subplot is inset with the histogram showing the difference of goodvisits values minus the combined spectra values.

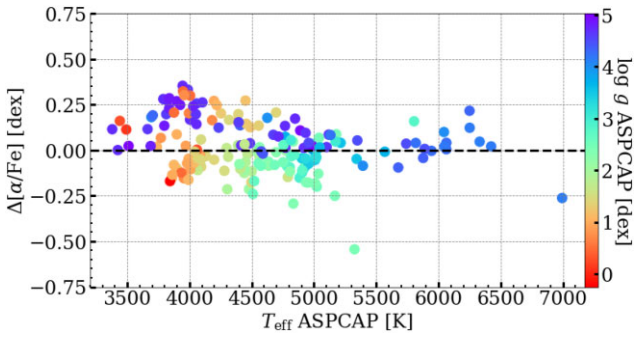

Figure 12. The difference in [α/Fe] when comparing the results of the stacked spectra with those from ASPCAP (our values minus ASPCAP).

the spectra that have $4000 < T_{\rm eff} < 5000$ K and $4 < \log g < 5$ are located in the CMD. Doing so suggests that this parameter combination is slightly undersampled in the MaStar survey. Fitting theoretical isochrones Bressan et al. (2012) to the CMD, as is done for our prior determination, and selecting the isochrone position closest to each data point, suggests that solar and super-solar stars are undersampled in this region. Once we remove spectra based on the quality flags described herein, the low density of points is further exaggerated. In summary, we suspect that the presence of heavy molecules in observed spectra and the undersampling of spectra in this parameter range are responsible for the lack of data points in this region.

Since the intention is to use these parameters to create SSP models, we want to know how well the theoretical stellar tracks are covered with different α enhancements. In Fig. 14 we show the HRD of recovered parameters binned by [α/Fe]. Overplotted are the theoretical isochrones from the Dartmouth Stellar Evolution Database (Dotter et al. 2008) for ages 1, 6, and 12 Gyr and approximately solar metallicity ([Fe/H] $= 0.07$).[4] From left to right, we vary the α-enhancement of the isochrones, such that: [α/Fe] $= -0.2$, 0 and 0.2 are used. This shows that we are able to produce SSP models for solar and super-solar [α/Fe], even though it is challenging to cover all of the parameter space in the latter. For the sub-solar [α/Fe] case it is not feasible, as expected. The solar scaled [α/Fe] models at high [Fe/H] and enhanced [α/Fe] models at low [Fe/H] for intermediate to old ages will be presented in a forthcoming paper (Maraston et al. in preparation).

5 CONCLUSIONS

In this paper, we build upon our previous efforts in Hill et al. (2022) to estimate stellar parameters for the final data release of the MaNGA Stellar Library (MaStar). As before, we derive fundamental stellar parameters from the MaStar observed spectra by comparing them to the theoretical stellar atmospheres from MARCS (Gustafsson et al. 2008) and BOSZ-ATLAS9 (Mészáros et al. 2012; Bohlin et al. 2017).

[4] http://stellar.dartmouth.edu/models/index.html

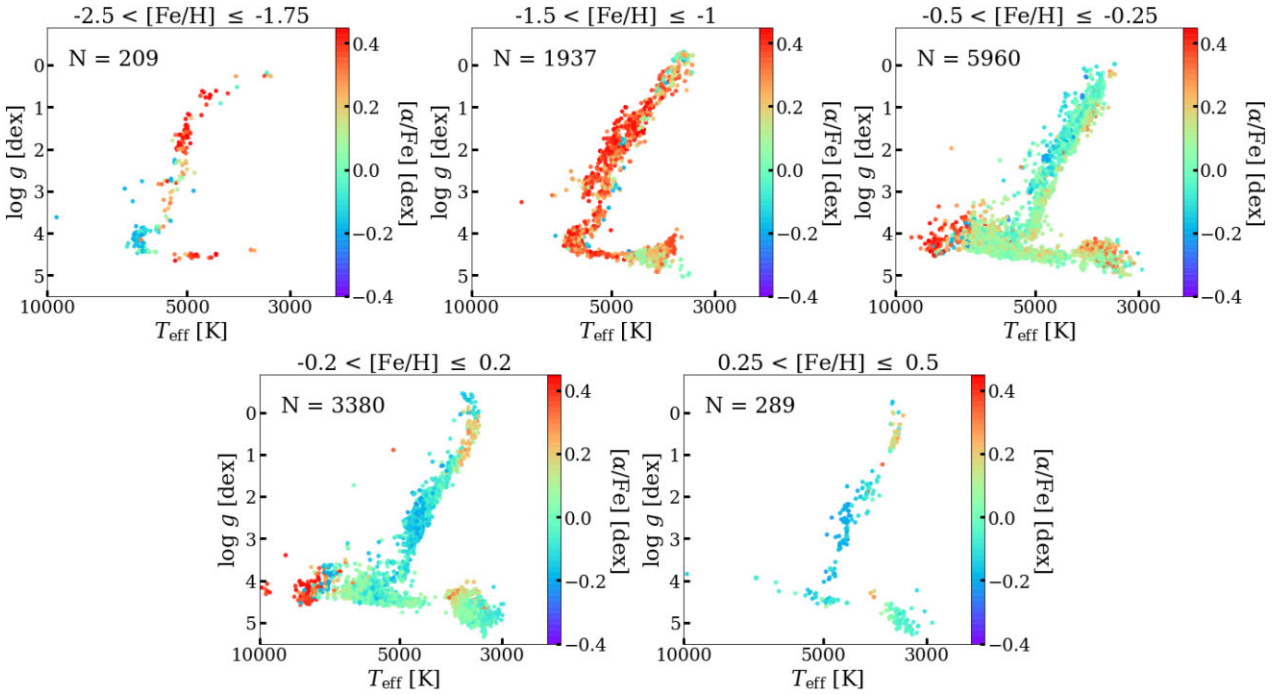

Figure 13. HR diagrams showing $T_{\rm eff}$ versus log g for the MaStar FSPs derived herein displaying five metallicity bins representing the progressive evolutionary history within the MW. The data points are coloured by our estimated [α/Fe] and the number of spectra within each bin is shown in the top left.

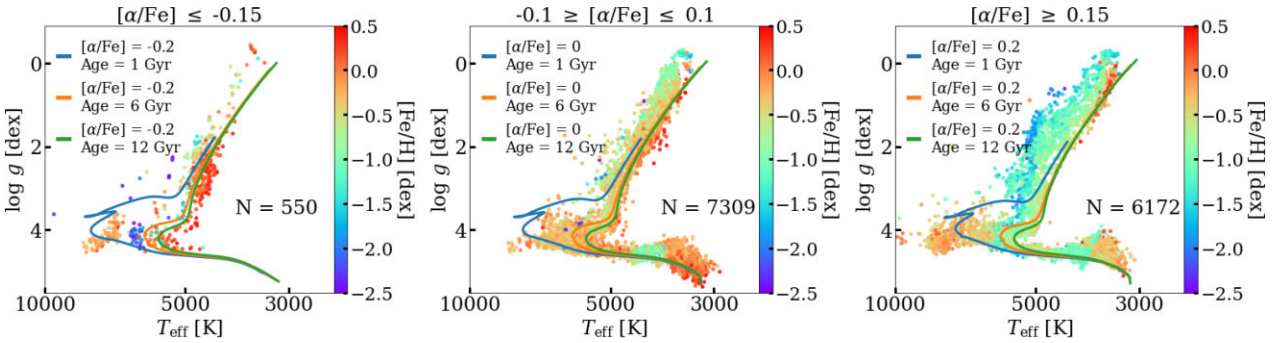

Figure 14. HR diagrams showing $T_{\rm eff}$ versus log g for the MaStar FSPs derived herein displaying three bins in [α/Fe]. The data points are coloured by our estimated [Fe/H] and the number of spectra within each bin is shown within each plot. Also plotted are the Dartmouth isochrones for 1, 6, and 12 Gyr. All isochrones have approximately solar metallicity, [Fe/H] = 0.07, and an increasing [α/Fe], from left to right: [α/Fe] = −0.2, 0, 0.2.

Through our full spectral fitting routine, using PPXF for continuum normalization and MCMC to map the parameter space, we can now estimate $T_{\rm eff}$, log g, [Fe/H], and [α/Fe] in parallel. For $T_{\rm eff}$ and log g, flat priors are used based on *Gaia* photometry and theoretical isochrones from Bressan et al. (2012), whereas [Fe/H] and [α/Fe] are prior free.

In addition to the quality cut based on the χ^2 measured from the best fit model and observed spectra, as used in H22, we implement additional quality measures for the use of [α/Fe]. Specifically, we now measure the integrated autocorrelation time of the MCMC chains every 50 iterations and only consider the chains converged when each parameter has reached 15 autocorrelation times and the parameter has changed by less than 1 per cent from the previous 50 iterations. Furthermore, spectra for which the average error of [α/Fe] is $\geq$0.22 are also flagged as invalid. These quality measures leave a total of 17 214 spectra with good quality fits in the range $-0.25 <$ [α/Fe] < 0.48. Applying quality cuts based on the MCMC convergence and the χ^2 fit only, we obtain the fundamental stellar parameters in the following ranges: $2913 \leq T_{\rm eff} \leq 26,096$ K, $-0.5 \leq \log g \leq 5.4$, $-2.5 \leq$ [Fe/H] ≤ 0.7. This parameter distribution is presented in Fig. 4.

With the strict quality cut for [α/Fe], we compare our results to those obtained with the ASPCAP (García Pérez et al. 2016; Jönsson et al. 2020), with Imig et al. (2022) and with the results obtained by the GSP-Spec algorithm for *Gaia* observations (Creevey et al. 2022; Fouesneau et al. 2022). The comparison with ASPCAP and Imig et al. (2022) was very informative as it revealed a degeneracy in our estimation of [α/Fe] that was strongest for log $g > 4.0$ and correlated with temperature, particularly in the range $3500 \leq T_{\rm eff} \leq 4500$ K (Fig. A1). We tested whether running the MCMC chains for longer and with more walkers would resolve this degeneracy, however it was mainly unsuccessful (Fig. A2). In Section A2 (see the Appendix), we then derive an alternative set of [α/Fe] values calibrated with the ASPCAP results.

Plotting the relationship between our estimated [Fe/H] and [α/Fe] in Fig. 7 shows a clear negative correlation; this is in agreement with

our understanding of the MW's chemical abundance pattern. The sky distribution of [α/Fe] is then shown in Fig. 8, showing a preference towards α enhancement in the halo.

To see whether [α/Fe] improves with higher S/N, we analyse the stacked and LSF homogenized spectra. An increased S/N produces cleaner spectra for the use in SSP models and allows for a more accurate parameter estimation, particularly for $T_{\rm eff}$ and [Fe/H]. However, the results shown by Figs 11 and 12 reveal that our estimation of [α/Fe] does not improve with S/N, at least to a median S/N of 119.

Finally, in Fig. 13 we have shown the distribution of [α/Fe] in HRDs of varying [Fe/H], based on the bins used for creating stellar populations models in Maraston et al. (2020). This demonstrates that we are able to cover most stellar types in the range of $-1.5 <$ [Fe/H] ≤ 0.2, with some inconsistencies at solar [Fe/H], $T_{\rm eff} \sim 4000$ K. We then plot the HRDs again, but in bins of [α/Fe] representing α-poor, solar-scaled, and α-enhanced populations. By overplotting theoretical isochrones, we are able to appreciate how these spectra can be used for the development of SSP models with a variable α enhancement.

ACKNOWLEDGEMENTS

LH acknowledges support from the Science & Technology Facilities Council (STFC) as well as the Data Intensive Science Centre in SEPnet (DISCnet). STFC is also acknowledged by JN for support through the Consolidated Grant Cosmology and Astrophysics at Portsmouth, ST/S000550/1. RY and DL acknowledge support by NSF grant AST-1715898. Numerical computations were done on the Sciama High Performance Compute (HPC) cluster which is supported by the ICG, SEPNet, and the University of Portsmouth.

RY acknowledges support by the Hong Kong Global STEM Scholar scheme, the Direct Grant of CUHK Faculty of Science, and by the Research Grant Council of the Hong Kong Special Administrative Region, China (Projects No. 14302522).

Funding for the Sloan Digital Sky Survey IV (SDSS-IV) has been provided by the Alfred P. Sloan Foundation, the U.S. Department of Energy Office of Science, and the Participating Institutions. SDSS-IV acknowledges support and resources from the Center for High Performance Computing at the University of Utah. The SDSS website is www.sdss.org.

SDSS-IV is managed by the Astrophysical Research Consortium for the Participating Institutions of the SDSS Collaboration including the Brazilian Participation Group, the Carnegie Institution for Science, Carnegie Mellon University, Center for Astrophysics | Harvard & Smithsonian, the Chilean Participation Group, the French Participation Group, Instituto de Astrofísica de Canarias, The Johns Hopkins University, Kavli Institute for the Physics and Mathematics of the Universe (IPMU) / University of Tokyo, the Korean Participation Group, Lawrence Berkeley National Laboratory, Leibniz Institut für Astrophysik Potsdam (AIP), Max-Planck-Institut für Astronomie (MPIA Heidelberg), Max-Planck-Institut für Astrophysik (MPA Garching), Max-Planck-Institut für Extraterrestrische Physik (MPE), National Astronomical Observatories of China, New Mexico State University, New York University, University of Notre Dame, Observatário Nacional / MCTI, The Ohio State University, Pennsylvania State University, Shanghai Astronomical Observatory, United Kingdom Participation Group, Universidad Nacional Autónoma de México, University of Arizona, University of Colorado Boulder, University of Oxford, University of Portsmouth, University of Utah, University of Virginia, University of Washington, University of Wisconsin, Vanderbilt University, and Yale University.

DATA AVAILABILITY

The data underlying this article can be accessed through the official SDSS-IV DR17 site: https://www.sdss.org/dr17/mastar/.

REFERENCES

Abdurro'uf et al., 2022, ApJS, 259, 35
Allende Prieto C., Koesterke L., Hubeny I., Bautista M. A., Barklem P. S., Nahar S. N., 2018, A&A, 618, A25
Aller L. H., Greenstein J. L., 1960, ApJS, 5, 139
Bailer-Jones C. A. L., Rybizki J., Fouesneau M., Demleitner M., Andrae R., 2021, AJ, 161, 147
Blanton M. R. et al., 2017, AJ, 154, 28
Bohlin R. C., Mészáros S., Fleming S. W., Gordon K. D., Koekemoer A. M., Kovács J., 2017, AJ, 153, 234
Bressan A., Marigo P., Girardi L., Salasnich B., Dal Cero C., Rubele S., Nanni A., 2012, MNRAS, 427, 127
Bundy K. et al., 2015, ApJ, 798, 7
Cappellari M., 2017, MNRAS, 466, 798
Cappellari M., Emsellem E., 2004, PASP, 116, 138
Chen Y.-P. et al., 2020, ApJ, 899, 62
Creevey O. L. et al., 2022, preprint (arXiv:2206.05864)
Dotter A., Chaboyer B., Jevremović D., Kostov V., Baron E., Ferguson J. W., 2008, ApJS, 178, 89
Drory N. et al., 2015, AJ, 149, 77
Duong L., Asplund M., Nataf D. M., Freeman K. C., Ness M., Howes L. M., 2019, MNRAS, 486, 3586
Foreman-Mackey D., Hogg D. W., Lang D., Goodman J., 2013, PASP, 125, 306
Fouesneau M. et al., 2022, preprint (arXiv:2206.05992)
Fu X., Bressan A., Marigo P., Girardi L., Montalbán J., Chen Y., Nanni A., 2018, MNRAS, 476, 496
Gaia Collaboration, 2021, A&A, 649, A1
García Pérez A. E. et al., 2016, AJ, 151, 144
Gonzalez O. A. et al., 2011, A&A, 530, A54
Goodman J., Weare J., 2010, Commun. Appl. Math. Comput. Sci., 5, 65
Green G. M., Schlafly E., Zucker C., Speagle J. S., Finkbeiner D., 2019, ApJ, 887, 93
Greggio L., Renzini A., 1983, Mem. Soc. Astron. Italiana, 54, 311
Gunn J. E. et al., 2006, AJ, 131, 2332
Gustafsson B., Edvardsson B., Eriksson K., Jørgensen U. G., Nordlund Å., Plez B., 2008, A&A, 486, 951
Hayden M. R. et al., 2015, ApJ, 808, 132
Hill L. et al., 2022, MNRAS, 509, 4308 (H22)
Imig J. et al., 2022, AJ, 163, 56
Jönsson H. et al., 2020, AJ, 160, 120
Law D. R. et al., 2015, AJ, 150, 19
Law D. R. et al., 2016, AJ, 152, 83
Law D. R. et al., 2021, AJ, 161, 52
Lee Y. S. et al., 2008a, AJ, 136, 2022
Lee Y. S. et al., 2008b, AJ, 136, 2050
Lee Y. S. et al., 2011, AJ, 141, 90
Maraston C., 1998, MNRAS, 300, 872
Maraston C., 2005, MNRAS, 362, 799
Maraston C., Greggio L., Renzini A., Ortolani S., Saglia R. P., Puzia T. H., Kissler-Patig M., 2003, A&A, 400, 823
Maraston C. et al., 2020, MNRAS, 496, 2962
Matteucci F., 1994, A&A, 288, 57
Mészáros S. et al., 2012, AJ, 144, 120
Nanni L. et al., 2022, MNRAS, 515, 320
Navarro J. F., Abadi M. G., Venn K. A., Freeman K. C., Anguiano B., 2011, MNRAS, 412, 1203
Ness M., Freeman K., 2016, PASA, 33, e022
Neumann J. et al., 2022, MNRAS, 513, 5988
Nissen P. E., Christensen-Dalsgaard J., Mosumgaard J. R., Silva Aguirre V., Spitoni E., Verma K., 2020, A&A, 640, A81
Nomoto K., Thielemann F. K., Yokoi K., 1984, ApJ, 286, 644

Pietrinferni A., Cassisi S., Salaris M., Castelli F., 2006, ApJ, 642, 797
Salasnich B., Girardi L., Weiss A., Chiosi C., 2000, A&A, 361, 1023
Thomas D., Greggio L., Bender R., 1999, MNRAS, 302, 537
Thomas D., Maraston C., Bender R., 2003, MNRAS, 339, 897
Thomas D., Maraston C., Bender R., Mendes de Oliveira C., 2005, ApJ, 621, 673
Tinsley B. M., 1979, ApJ, 229, 1046
Tinsley B. M., 1980, Fund. Cosmic Phys., 5, 287
VandenBerg D. A., Swenson F. J., Rogers F. J., Iglesias C. A., Alexander D. R., 2000, ApJ, 532, 430
Venn K. A., Irwin M., Shetrone M. D., Tout C. A., Hill V., Tolstoy E., 2004, AJ, 128, 1177
Wallerstein G., 1962, ApJS, 6, 407
Xiang M. et al., 2022, A&A, 662, A66
Yan R. et al., 2016a, AJ, 151, 8
Yan R. et al., 2016b, AJ, 152, 197
Yan R. et al., 2019, ApJ, 883, 175
Yanny B. et al., 2009, AJ, 137, 4377

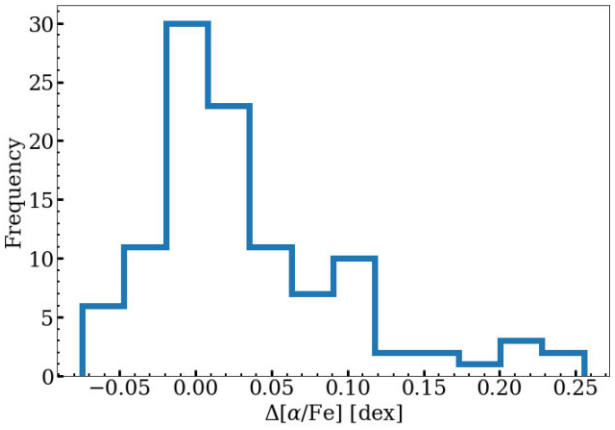

Figure A2. Histogram showing the difference in [α/Fe] when using the automatic convergence method and running the MCMC for 5000 iterations with 200 walkers (automatic method minus 5000 iteration test), for a subset of spectra that have a higher estimated [α/Fe] than ASPCAP by at least 0.25 dex.

APPENDIX: ASPCAP DISCREPANCY

A1 Investigation

To understand the source of the discrepancy for log g > 4.0, we examine the chains using corner plots which reveal the marginalized posterior density for each parameter and the covariance between parameters. The left-hand panel of Fig. A1 shows an example corner plot for one observation where a degeneracy in [α/Fe] is present and the lower, more physical value of [α/Fe], given the chosen [Fe/H], is adopted. In the right-hand panel, a star with similar parameters is shown, but the larger value of [α/Fe] is adopted. The determination of [α/Fe] is not well constrained for this combination of FSPs and a degeneracy is present, despite being considered as converged by our quality checks. Taking the first peak at [α/Fe] ∼0.16 would significantly reduce the difference with ASPCAP, who recover [α/Fe] = −0.04 for this star. Such behaviour is commonly found for this combination of FSPs in our catalogue and could be explained by the walkers getting stuck in a local minimum. We have confidence in the parameter estimation of ASPCAP in this domain since the average value for [α/Fe] we find at [Fe/H] ∼−0.4 is too high for typical MW stars at this metallicity.

To try and improve our estimation of [α/Fe] for these spectra we run our MCMC analysis for 5000 iterations and increase the number of walkers to 200 in order to allow walkers to move out of local minima. We select 108 spectra for 62 stars where the difference in [α/Fe] with ASPCAP is greater than 0.25 dex. For the original analysis of these selected spectra it took, on average, 811 iterations for all four parameters to be considered as converged. In Fig. A2, we show a histogram of the differences between the original MCMC result for [α/Fe] minus the results from this test with 5000 iterations

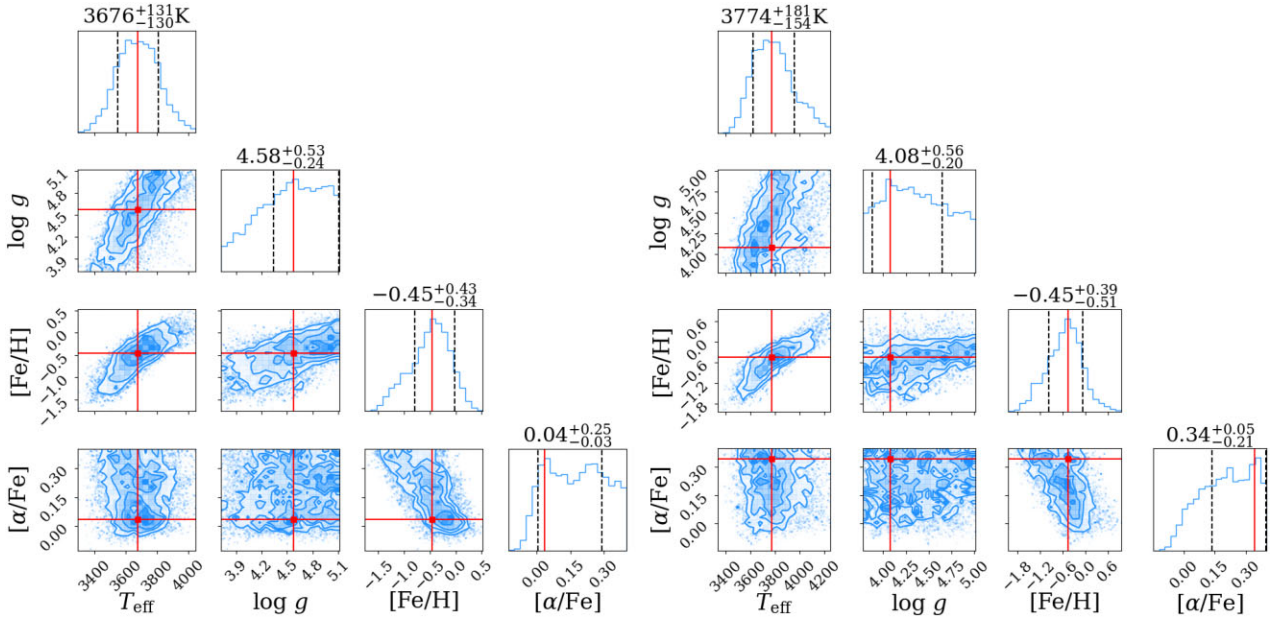

Figure A1. *Left*: Corner plot for MaNGA ID 60-3314329097279891584 showing the posterior distribution for each atmospheric parameter. The posterior for [α/Fe] shows a degeneracy that is commonly found in our parameter estimation for sub-solar, cool dwarfs. This is an example where the estimated [α/Fe] makes sense, given [Fe/H]. *Right*: Corner plot for MaNGA ID 3-146794027. This shows a similar star to the left-hand panel, but an overestimated [α/Fe]. The ASPCAP value for this star is [α/Fe] = −0.04.

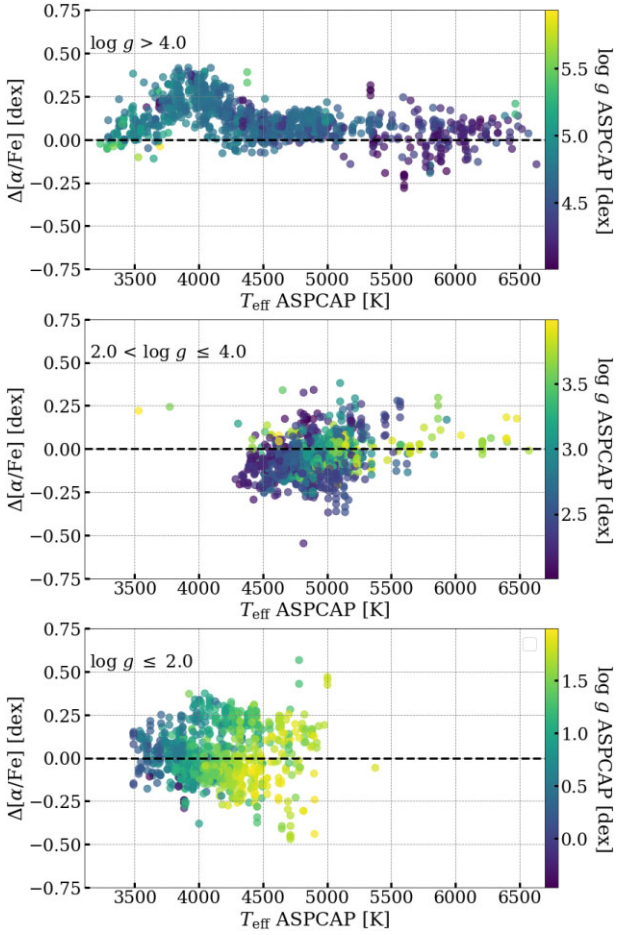

Figure A3. Comparison of the [α/Fe] values presented in this work and those from ASPCAP. In each panel, we show the difference (this work minus ASPCAP) in [α/Fe] as a function of $T_{\rm eff}$ from ASPCAP, split into three bins based on log g: log $g > 4$, $2 < \log g \leq 4$, log $g \leq 2$.

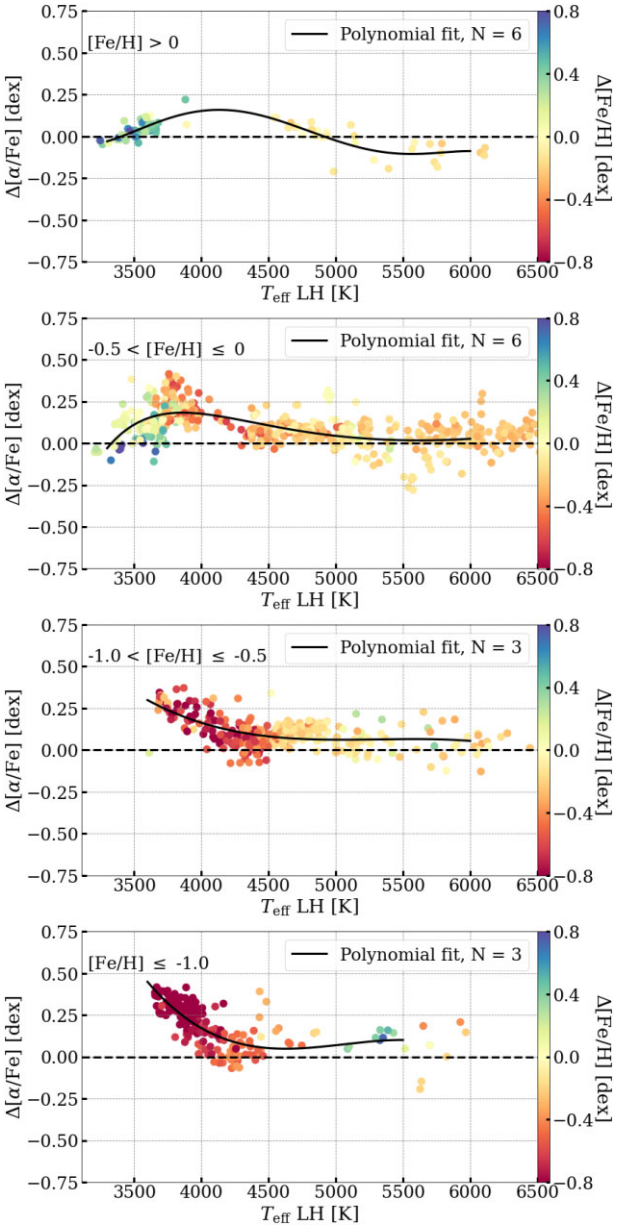

Figure A4. Comparison of the [α/Fe] values presented here minus those from ASPCAP as a function of our $T_{\rm eff}$, points are coloured by our [Fe/H] minus ASPCAP's. Each panel shows different bins in [Fe/H] from our analysis, where we estimate log $g > 4.0$. The solid black line in each plot shows the polynomial fit to the differences with the polynomial order (N) shown in the legend.

and 200 walkers. There is a preference to lower values of [α/Fe] with the extended iterations. However, 35 per cent of the results moved further away from the ASPCAP value. We conclude that in this parameter range, the MaStar resolution and wavelength window may be limiting factors when comparing to theoretical models.

A2 Calibration

Since we cannot resolve the degeneracy, we provide an alternative parameter set for [α/Fe] which is calibrated using ASPCAP's parameters. We place trust in the ASPCAP value of [α/Fe] since they work at a much higher resolution than MaStar.

To see how [α/Fe] compares for different spectral types, the comparison with ASPCAP is performed for three log g bins, as shown in Fig. A3. The x-axis shows $T_{\rm eff}$ as derived by ASPCAP and the y-axis is the [α/Fe] presented in this work minus ASPCAP's. In the high log g bin (log $g > 4.0$), the discrepancy in [α/Fe] is clearly correlated with $T_{\rm eff}$, peaking at approximately 3900 K. A smaller offset is observed in the intermediate log g bin ($2.0 < \log g \leq 4.0$) at $4300 < T_{\rm eff} < 4700$ K. In the lowest log g bin (log $g \leq 2.0$), the differences are centred around zero with no correlation.

To mitigate this overestimation in [α/Fe] for cool dwarfs stars we calibrate our result with ASPCAP (see Fig. A4). Since [α/Fe] and [Fe/H] are inherently related, we further split our comparison with ASPCAP for the log $g > 4.0$ bin into four bins based on [Fe/H]: [Fe/H] > 0.0, $-0.5 <$ [Fe/H] ≤ 0.0, $-1.0 <$ [Fe/H] ≤ -0.5, $-1.5 <$ [Fe/H] ≤ -1.0. The comparison is now presented in terms of the FSPs presented in this paper, rather than ASPCAP's, since our FSPs are not equal which would lead to an incorrect calibration. We colour each data point by our estimated [Fe/H] minus ASPCAP's, since we want to avoid calibrating [α/Fe] where Δ[Fe/H] is significant. This plot gives similar trends to the top panel of A3, with the largest discrepancy now at lower $T_{\rm eff}$. This is not surprising

since we tend to slightly underestimate $T_{\rm eff}$ compared to ASPCAP, as shown in figure 15 of H22. Furthermore, in the lower [Fe/H] bins, the difference between our value of [Fe/H] and ASPCAP's increases, as we generally estimate a lower [Fe/H] for this log g at low $T_{\rm eff}$.

In order to calibrate values, we use a least squares polynomial fit to model the differences in each [Fe/H] bin and use each to correct spectra in our catalogue that have log $g > 4$ and fall within each bin. Furthermore, to ensure that we calibrate only where our [Fe/H] values are similar with ASPCAP, we also impose that $|\Delta$[Fe/H]$| < 0.5$. The order of the polynomial is shown in each subplot and was chosen to reduce overfitting but also to capture the overall trend of the offset within each bin. To avoid issues from extrapolating to lower temperatures, we only calibrate the parameters where $T_{\rm eff}$ is within the range that the polynomial is modelled. This mainly affects the most metal-poor population of stars; however, our catalogue of parameters does not contain such cool, metal-poor examples. For the high temperature spectra, we are less concerned since our estimation of [α/Fe] is consistent with ASPCAP here. Applying this calibration alters the [α/Fe] value for 41 per cent of the spectra once applying the strict flag conditions.

These calibrated parameters can be downloaded from https://www.icg.port.ac.uk/mastar/.

This paper has been typeset from a TEX/LATEX file prepared by the author.